MIJST
MIST International Journal of Science and Technology

Impact of Inverter Control and Solar Photovoltaic Integration on Small Signal Stability Augmented with Battery: Modal Analysis Approach

Md. Mahadi Hasan*, Md. Imranul Hasan Emon, Hasan Monir, and Md Ahsan Kabir

Department of EECE, Military Institute of Science and Technology, Dhaka, Bangladesh

***Corresponding Email:** *mahadi_hasan@eece.mist.ac.bd*

ARTICLE INFO

Article History:

Received: 11th April 2025
Revised: 18th October 2025
Accepted: 19th October 2025
Published: 30th December 2025

Keywords:

Small Signal Stability; Inertia; Battery; Solar Photovoltaic; Modal Analysis; Inverter

ABSTRACT

The increasing penetration of renewable energy sources, particularly solar photovoltaic (PV), poses significant challenges to grid stability due to the reduction in system inertia. This paper evaluates three inverter control strategies—$\boldsymbol{V_{ac}-\Phi}$, $\boldsymbol{V_{ac}-P}$, and $\boldsymbol{P-Q}$ —using modal analysis and participation matrix evaluation to identify the most effective approach for enhancing small signal stability. Among these, the $\boldsymbol{P-Q}$ control strategy emerges as the best-performing technique, with a notable eigenvalue improvement from $\boldsymbol{-0.62+9.607i}$ $(\boldsymbol{V_{ac}-\Phi})$ to $\boldsymbol{-14.79+0.668i}$, achieving an exceptionally high damping ratio of 0.998. The participation matrix analysis highlights the dominance of active power control in stabilizing critical modes, further validating the superior performance of $\boldsymbol{P-Q}$ control. Moreover, the impact of solar PV has been demonstrated and enhancement of system stability utilizing Battery Energy Storage System (BESS) has been shown in this paper.

1. INTRODUCTION

1.1 State of the Art

The integration of Renewable Energy Sources (RES) into modern power grids has emerged as a critical strategy to address global energy demands while mitigating environmental impact. It plays a pivotal role in decarbonization, aligning with international climate change mitigation goals by reducing reliance on traditional fossil fuel power plants (Kåberger, 2018), (Ram et al., 2018), (International Renewable Energy Agency, 2022). Among the diverse RES technologies—solar photovoltaic (PV), hydropower, wind power, geothermal energy, biomass energy, concentrated solar power, and ocean energy—solar PV has gained unprecedented momentum as the global energy landscape shifts toward renewables. According to the REN21 report, solar PV accounted for 70% of all new renewable capacity additions in 2022, a trend driven by declining costs, modularity, and accessibility compared to alternative resources (Renné,2022), (REN21, 2023), (McGinn et al., 2013). The combination of falling prices and growing demand has established solar PV as the most cost-effective and desirable RES technology (Chong et al., 2024), (Lu et al., 2021), (Wiser et al., 2017), (Roser, 2020). However, integrating solar PV into existing grid infrastructures presents challenges due to its intermittent and unpredictable nature, as well as the nonlinear characteristics of power converters (Tavakoli et al., 2020), (Kiasari et al., 2024), (Hamid et al., 2023), (Aljarrah et al., 2024), (Hamid et al., 2023). These challenges, particularly pronounced at high penetration levels, can affect grid reliability, stability, and power quality, resulting in issues such as voltage sag, flicker, harmonics, and unbalance (Ali et al., 2024), (Pandey & Prasad, 2024). Modern grid codes have been established to mitigate these challenges, requiring features such as dynamic active power regulation, reactive power support, fault ride-through capabilities, harmonic compliance, and cybersecurity measures to ensure the smooth integration of large-scale PV power plants (Boscaino et al., 2024), (Jamal et al., 2017). Battery Energy Storage Systems (BESS) play a critical role in this integration by addressing the variability of PV output. BESS stores excess energy during peak generation and releases it during periods of deficit, enabling optimal system performance and cost- effectiveness (Shivashankar et al., 2016), (Makarov et al., 2008).

1.2 Literature Review

Recent research highlights various strategies for integrating PV and BESS into power grids,

emphasizing inverter-based control methods for enhancing stability and power quality. A genetic algorithm-based approach was proposed in (Gali et al., 2023) to optimize BESS sizing, while (Emrani et al., 2024) developed a day-ahead dispatch model for hybrid PV–wind–BESS systems. Rule-based BESS controllers (Teleke et al., 2010) and power management schemes using moving average filtering (Koohi-Kamali et al., 2014) improved PV output regulation, and Hill et al. (Hill et al., 2012) recommended centralized BESS for voltage and frequency support. Daud et al. (Daud et al., 2012) demonstrated the superiority of lithium-ion batteries for grid-tied PV systems. Other studies (Teng et al., 2012; Akatsuka et al., 2010) applied optimization and hybrid control to minimize losses and stabilize converter outputs. Research in (Zeng et al., 2006; Biroon et al., 2020) analyzed advanced BESS control loops for improved dynamic stability, and (Das & Aliprantis, 2008), (Alias & Singh, 2021), (Iyer et al., 2018), (Muriuki et al., 2016),(Shaw & Kumar, 2016) examined small-signal behavior and damping enhancement through active power, voltage, and reactive power ($P-Q$ and $V-P$) control. Collectively, these works establish the relevance of inverter control strategies—particularly $V_{ac}-\Phi$, $V_{ac}-\mathrm{P}$, and $P-Q$ —for small-signal stability improvement in PV- and BESS integrated systems.

1.3 Research Gap and Paper Contributions

Despite significant progress in addressing RES integration challenges, the impact of inverter control strategies on system stability remains underexplored. Modal analysis has been widely adopted to evaluate small-signal stability, providing detailed insights into system dynamics and control effectiveness [38–40]. However, systematic comparisons of control strategies like $V_{ac}-\Phi$, $V_{ac}-\mathrm{P}$, and $P-Q$ under varying operating conditions are limited especially under scenarios of increasing PV penetration, leaving gaps in understanding their dynamic stability impacts.

This paper addresses these gaps with the following contributions:

- An in-depth comparative study of three key inverter control algorithms—$V_{ac}-\Phi$, $V_{ac}-\mathrm{P}$, and $P-Q$ —using modal analysis to assess their effectiveness in simulating virtual inertia and improving small-signal stability.
- A detailed investigation into the impacts of increasing PV penetration on the stability of a modified 9-bus test system.
- An evaluation of the role of BESS in enhancing system stability, focusing on eigenvalue shifts, participation factors, and their implications for mitigating reduced inertia caused by high-RES penetration.
- An integrated assessment of inverter control strategies and BESS on frequency regulation to provide insights into optimal configurations for grid resiliency.

The paper begins with an introduction in Section 1. Section 2 outlines the methodology adopted for this study, followed by the simulation setup described in Section 3. Section 4 presents the software simulation results, which are discussed in detail in Section 5. Finally, the paper concludes with the key findings summarized in Section 6.

2. MATERIALS AND METHODS

2.1 Modal analysis

Small-signal stability refers to the ability of a power system to maintain synchronism and return to steady state following small disturbances such as load or generation fluctuations. It primarily depends on the location of eigenvalues of the system's linearized dynamic model. If all eigenvalues possess negative real parts, system modes are stable; eigenvalues near the imaginary axis indicate weak damping and oscillatory behavior. The damping ratio associated with each mode quantifies the rate at which oscillations decay. Participation factors further identify the state variables most responsible for specific modes, linking control loops or devices (e.g., inverters, generators, or BESS) to dominant oscillations.

Therefore, small-signal stability analysis is a powerful tool for understanding the dynamic interactions in converter-based renewable systems and assessing the effectiveness of control strategies such as $V_{ac}-\Phi$, $V_{ac}-\mathrm{P}$, and $P-Q$ control. For small-signal stability analysis the general form of power system mathematical model is linearized (Vetoshkin & Müller, 2021). Hence, the linear form of the model is shown in equation (1).

$$\Delta x = A\Delta x + B\Delta v \tag{1}$$

where Δx is the state vector of the power system, A is the system matrix corresponding to devices constants and B is the input matrix that correlates with node voltages. The power flow in the network is described by equation (2):

$$\Delta \mathrm{i} = y_{\mathrm{N}}\Delta v \tag{2}$$

where, Y_N network admittance matrix and $\Delta \mathrm{i}$ is the vector of current injections The current injection is defined as equation (3):

$$\Delta \imath = C_{\mathrm{D}}\Delta x + D_{\mathrm{D}}\Delta v \tag{3}$$

where C_{D} and D_{D} is matrix corresponding to individual devices. This simplifies to equation (4):

$$Y_{\mathrm{N}}\,\Delta v = C_{\mathrm{D}}\,\Delta x + D_{\mathrm{D}}\,\Delta v \tag{4}$$

Then the solution for the vector of voltages is given as equation (5):

$$\Delta v = (Y_{\mathrm{N}} - D_{\mathrm{D}})^{-1} C_{\mathrm{D}}\,\Delta x \tag{5}$$

Hence, the system of differential-algebraic equations becomes the system of only differential equations as (6):

$$\Delta x = A\,\Delta x + B\,(Y_N - D_D)^{-1}\,C_D\,\Delta x \quad (6)$$

Consequently, $A_{sys} = A + B\,(Y_N - D_D)^{-1}\,C_D$ is new system matrix with reduced algebraic equation. Thus, the small-signal stability can be analyzed by finding the eigenvalues of A_{sys}. Furthermore, the damping ratio ζ_i of individual eigenvalues might be evaluated using the following formula-(7):

$$\zeta_i = \frac{\sigma_i}{\sqrt{\sigma_i^2 + w_i^2}} \quad (7)$$

where the assumed form of the i_{th} eigenvalue is $\lambda_i = \sigma_i + j\omega_i$. The eigenvalues of the system matrix obtained by previous computations are then used for comparing the stability of examined strategies. The Lyapunov indirect method provides insights into the system dynamics, where the system's ability to return to steady-state after a disturbance is determined by *max* (Re(λ)). The damping ratio predicts whether oscillations dampen quickly or persist over time. Additionally, the participation factors for individual modes are calculated using equation-(8):

$$P_{k,i} = \frac{|\omega_{k,i}||v_{k,i}|}{\sum_{k=1}^{n}|\omega_{k,i}||v_{k,i}|} \quad (8)$$

where $\omega_{k,i}$ and $v_{k,i}$ are components of left and right eigenvectors corresponding to i_{th} eigenvalue. The sum of all participation factors for individual modes equals unity.

Voltage source converter (VSC)

The VSC operates in either $P-V$ or $P-Q$ control mode. In $P-V$ control mode, the converter regulates active power (P) and voltage (V), while in $P-Q$ control mode, it manages fixed active power (P) and reactive power (Q). For this study, the reactive power in $P-Q$ mode is set to zero.

In grid-connected operation, inverter controls are implemented within the VSC framework using the synchronous $\boldsymbol{d-q}$ reference frame. The $\boldsymbol{V_{ac}-\Phi}$ (voltage–phase) control modulates the converter's terminal voltage magnitude to influence the phase angle between converter and grid voltages, thereby regulating active power flow across the coupling reactance—an approach commonly used in weak-grid or microgrid conditions where voltage–angle dynamics dominate power transfer. The $\boldsymbol{V_{ac}-P}$ (voltage–power) control simultaneously regulates voltage and active power, making it suitable for distribution-level PV inverters that must maintain bus voltage while supporting power balancing. In contrast, the $\boldsymbol{P-Q}$ (active–reactive power) control fully decouples real and reactive power through the $\boldsymbol{d-q}$ current components, enabling fast and independent regulation. This approach is most widely used in grid-tied converters and BESS systems, as it ensures compliance with grid-support requirements such as voltage regulation, reactive power injection, and dynamic stability enhancement. The summary of the inputs and outputs of the three control strategies are given in Table 1.

Table 1: Comparative Summary of Control Strategies

1. Control Mode	2. Controlled Variables	3. Inputs	4. Outputs
5. $V_{ac}-\Phi$	6. Voltage amplitude (V_{ac}) & phase angle (Φ)	7. V_{ref}, Φ_{ref}	8. Converter voltage magnitude
9. $V_{ac}-P$	10. Voltage amplitude & active power	11. V_{ref}, P_{ref}	12. V, P
13. $P-Q$	14. Active and reactive power	15. P_{ref}, Q_{ref}	16. i_d, i_q

2.2.1 PV Control

The P-V controller consists of an active power control loop and a voltage control loop. In (DIgSILENT, 2011), the control system as it appears in Power Factory is presented. In the model, the parameters can be varied to tune the converter to present the desired transient response. The active and voltage control loops are modeled as PI controllers in the $d-q$ reference frame, where active power is primarily regulated through the d-axis current and voltage magnitude through the q-axis current reference (Jerkø, 2014).

2.2.2 Active power control loop

The active power control loop is based on a PI controller and decides the active power output of the converter. The active power loop is illustrated in Figure 1.

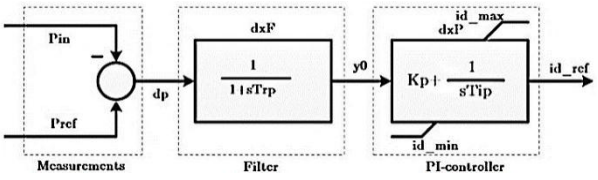

Figure 1: Active power control loop.

The first block in the illustration above measures the active power in (P_{in}) and computes the error ($d_p = P_{ref}$-P_{in}). P_{ref} is the active power reference which can be controlled in per unit. The second block represents a low pass filter with the cut-off frequency as the parameter. T_{rp} is the filter time constant for the active path, and it is a function of the cut-off frequency.

The third block represents a PI controller with defined maximum and minimum limits. This

controller comprises a proportional gain, k_p , and an integrator time constant, T_{ip} . The current in the d-axis, $i_{d,ref}$, is the parameter limiting the active power. In the simulation events, the active power can be fixed at a desired value by controlling $i_{d,ref}$. $i_{d,ref}$ is applied to an internal controller which produces the pulse width modulations (P_{md}) in the d-axis as show in Figure 2.

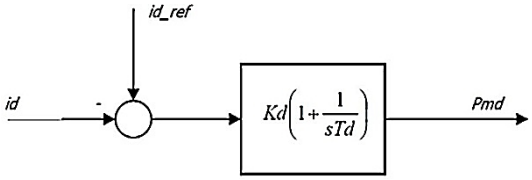

Figure 2: Block diagram of the built-in current controller in the d-axis (DIgSILENT, 2011).

The input currents to the controller are the AC-currents expressed in a reference frame defined by an input signal, cos_{ref}. The output signal is defined in the same reference frame and transformed back to a global reference using the same cos_{ref}. If the built-in current controllers are all set to zero (k_p = 0, T_{ip} = 0, k_{iq} = 0, T_{iq}= 0), the controller is disabled and the converter output current, i_d , is equal to the input variable $i_{d,ref}$. Hence the PWM converter is operating as a current source (DIgSILENT, 2011). The Park Transformation, which describes the conversion from a three-phase sinusoidal signal into quantities in a two-axis reference, is presented in (DIgSILENT, 2011). In steady state analysis, d_p = $i_{d,ref}$ = 0. When the simulation is run with dynamic conditions, these parameters differ from zero, and PI control is performed until d_p is compensated.

2.2.3 Voltage control loop

17. The voltage control loop decides the voltage output of the converter. From the measurement blocks, Vin is measured using a special measuring device. V_{ref} is the controllable reference voltage, while dV is the voltage error. The second block in Figure 3 is the measurement filter, which is a low pass filter dependent on the cut-off frequency. The dead band with offset and limits contains the reactive current support characteristics. The dead band is set to zero in the simulations performed in this work.The last block, in the lower right corner of Figure 4, is a limited non-windup integrator which compensates for the error. This block also soothes out the response of the reactive current for large transients in the input voltage. $i_{q,ref}$ is, just like $i_{d,ref}$, applied to an internal PI controller which produces the q- axis pulse-width-modulations (P_{mq}).

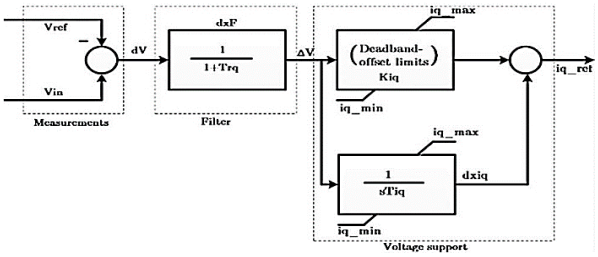

Figure 3: Voltage control loop.

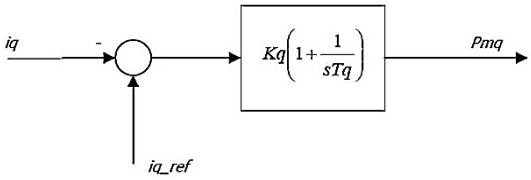

Figure 4: Block diagram of the built-in current controller in the q-axis (DIgSILENT, 2011).

where $k_i = sT_d$ which is integral gain and k_d is the proportional gain and τ_i is the time-constant usually it is in the range of 0.5 to 5 ms depending on the design speed then this can be expanded as shown in equation 9 & 10:

$$k_i = R/\tau_i \quad (9)$$

$$k_d = L/\tau_i \quad (10)$$

The reference frame defined by the input signal for the q- axis is given by sin_{ref} . Setting the built-in controllers to zero will lead to a converter output current, i_q , equal to the input variable $i_{q,ref}$ (Jerkø, 2014; DIgSILENT, 2011).

where $k_i = sT_d$ which is integral gain and k_d is the proportional gain and τ_i is the time-constant usually it is in the range of 0.5 to 5 ms depending on the design speed then this can be expanded as shown in equation 9 & 10:

$$k_i = R/\tau_i \quad (9)$$

$$k_d = L/\tau_i \quad (10)$$

The reference frame defined by the input signal for the q- axis is given by sin_{ref}. Setting the built-in controllers to zero will lead to a converter output current, i_q, equal to the input variable $i_{q,ref}$ (Jerkø, 2014; DIgSILENT, 2011).

3. RESULTS AND DISCUSSIONS

The simulation setup is based on the standard Western System Coordinating Council (WSCC) 3-machine, 9-bus test system, widely recognized for small-signal stability studies. The network comprises three two-winding transformers, six transmission lines, and three loads, with each synchronous generator modeled to include detailed voltage regulators, exciters, steam turbine–governor dynamics, and excitation systems. The generator operating conditions, which define the steady-state linearization point for modal analysis, are

summarized in Table 2. The negative reactive output of Gen 3 indicates absorption for voltage support, ensuring a realistic operating profile. These dispatch points serve as the initial equilibrium state for eigenvalue-based small-signal analysis. Time-domain simulations were conducted in DIgSILENT PowerFactory, with dynamic models implemented in DIgSILENT Simulation Language (DSL). The overall system configuration is shown in Figure 7.

Table 2. Generator operating conditions in the WSCC 9-bus system

Generator	Active Power (MW)	Reactive Power (MVar)	Rating (MVA)	PF
Gen 1	71.6	27.0	247.5	0.85
Gen 2	163.0	6.7	192.0	0.85
Gen 3	128.0	–10.9	128.0	0.85

4. SIMULATION RESULTS

This section presents three case studies on the WSCC 9-bus test system to evaluate its small-signal stability under varying conditions. Small-signal disturbances were introduced as ±5% step changes in the inverter control references—specifically, in the active power (P_{ref}) of the d-axis and voltage reference (V_{ref}) of the q-axis control loops at Bus 6, where PV and BESS units are integrated. The 0.1–0.5 seconds step duration simulated minor load fluctuations and control adjustments, keeping the system within the linear region for modal analysis. The resulting eigenvalues and participation factors were analyzed to assess damping and stability characteristics.

The first case study compares $V_{ac} - \Phi$, $V_{ac} - \mathrm{P}$, and $P - Q$ control modes, evaluating system performance through eigenvalue and damping ratio analysis across 19 modes and associated state variables. The second case study examines the effect of increasing PV penetration, highlighting reduced inertia and its influence on modal stability. The third case study explores BESS integration, showing how varying storage capacities enhance damping and mitigate low-inertia effects. Collectively, these studies provide a comprehensive evaluation of how inverter control, PV penetration, and BESS capacity influence the dynamic stability of the grid.

4.1 Case-I: Comparison among inverter control mode (i.e. $V_{ac} - \Phi, V_{ac} - P$ & $P - Q$) with fixed DC voltage source

In this study, a fixed DC voltage source was applied, followed by an inverter at bus 6, and three control modes— $V_{ac} - \Phi$, $V_{ac} - \mathrm{P}$, and $P - Q$ —were successively implemented to observe their impact on the stability of the system. The PV inverter at Bus 6 is modeled as a 60 MVA PWM converter (100 kV DC, 10 kV AC, 10% short-circuit impedance, 1.0 p.u. voltage reference) operating under sinusoidal modulation [Kiasari et al., 2024]. During small-signal disturbances, its $P - Q$ or $V_{ac} - \mathrm{P}$ control loops adjust the d–q current references within the linear modulation range, maintaining stable power injection and voltage support [(Hamid et al., 2023), (Aljarrah et al., 2024)]. Although its capacity is smaller than the synchronous generators of the WSCC system (247.5, 192.0, and 128.0 MVA)—approximately 24% of Gen3 and 31% of Gen2—the inverter's fast dynamic response enables it to provide disproportionately high damping and voltage regulation [Hamid et al., 2023]. Thus, the inverter acts as an active stability resource, with its rating and control strategy directly influencing eigenvalue trajectories, damping ratios, and modal participation, thereby enhancing small-signal stability in renewable-integrated power systems [(Ali et al., 2024), (Pandey & Prasad, 2024)]. The resulting eigenvalues, damping ratios, and eigenvalue plots are presented in Table 3 and Figure 5.

Table 3. Eigenvalue and damping ratio of different control conditions with constant voltage source

Mode No.	Control Condition	Eigen Value $\lambda i = \sigma i + J\omega_i$	Damping Ratio
3	$V_{ac} - \Phi$	$-0.62 + 9.607i$	0.063
	$V_{ac} - \mathrm{P}$	$-0.62 + 9.589i$	0.064
	$P - Q$	$-14.79 + 0.668i$	0.998
4	$V_{ac} - \Phi$	$-0.62 - 9.607i$	0.063
	$V_{ac} - \mathrm{P}$	$-0.62 - 9.589i$	0.064
	$P - Q$	$-14.79 - 0.668i$	0.998
5	$V_{ac} - \Phi$	$-0.52 + 6.195i$	0.083
	$V_{ac} - \mathrm{P}$	$-0.514 + 6.26i$	0.082
	$P - Q$	$-15 + 0.26i$	0.99
6	$V_{ac} - \Phi$	$-0.52 - 6.195i$	0.083
	$V_{ac} - \mathrm{P}$	$-0.514 - 6.26i$	0.082
	$P - Q$	$-15 - 0.26i$	0.99
7	$V_{ac} - \Phi$	$-14.48 + 0.5i$	0.99
	$V_{ac} - \mathrm{P}$	$-14.48 + 0.515i$	0.99
	$P - Q$	$-15.61 + 0.403i$	0.99
8	$V_{ac} - \Phi$	$-14.48 - 0.5i$	0.99
	$V_{ac} - \mathrm{P}$	$-14.48 - 0.515i$	0.99
	$P - Q$	$-15.61 - 0.403i$	0.99

Table 3 highlights the comparison of eigenvalues and damping ratios for the dominant modes, specifically modes 3, 4, 5, 6, and 8. The analysis reveals that the $V_{ac} - \Phi$ and $V_{ac} - \mathrm{P}$ control modes exhibit similar small-signal stability, as their eigenvalue positions are nearly identical. However, a significant shift in eigenvalues from the right to the left half-plane was

observed when the $P-Q$ control mode was applied, indicating an improvement in the system's inertial response and overall stability. Additionally, the damping ratio, a critical indicator of stability, showed a substantial increase under the P-Q control mode compared to the $V_{ac}-\Phi$ and $V_{ac}-\mathrm{P}$ modes, as summarized in Table 3.

P modes, as summarized in Table 3.

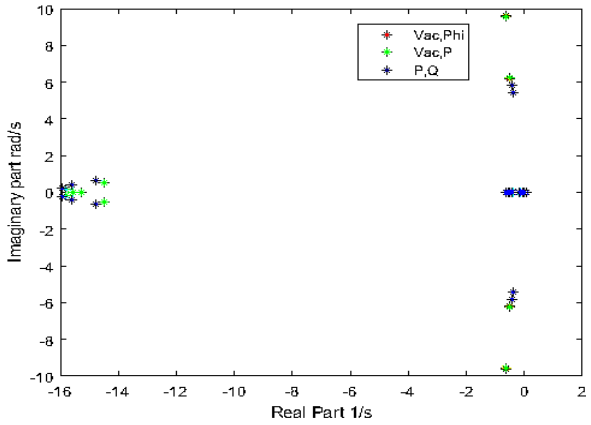

Figure 5: Eigenvalues plot in three control conditions with constant voltage source at Bus 6

Among the three control strategies, the maximum real part of the eigenvalues (Re(λ)) was observed under the $P-Q$ control mode, demonstrating its superior ability to handle stability challenges more effectively than the other modes. These findings underscore the effectiveness of the $P-Q$ control strategy in enhancing both small-signal stability and overall system performance.

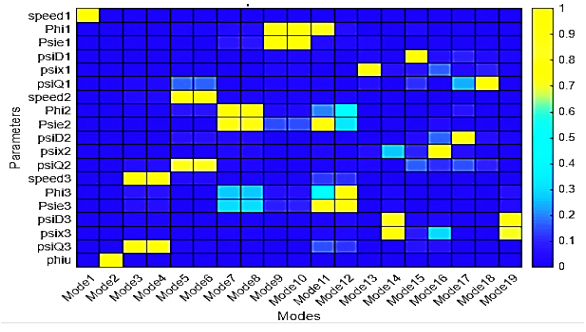

(a)

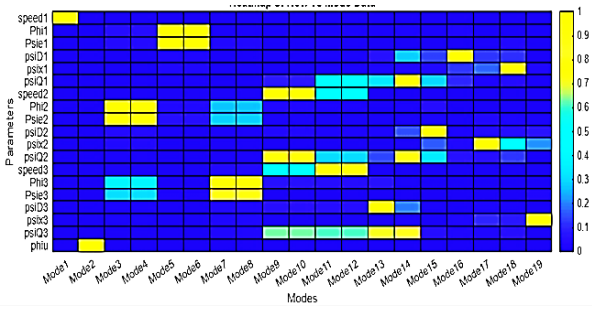

(b)

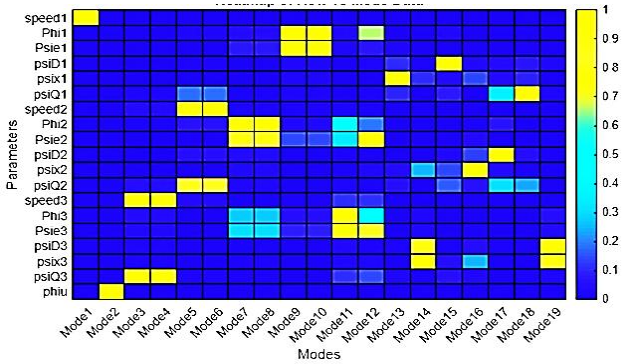

(c)

Figure 6: Matrix of participation factors under different control conditions with constant Voltage source (a) $V_{ac}-\Phi$ (b) $V_{ac}-\mathrm{P}$ and (c) $P-Q$

The participation matrices, represented in Figure 6 (a) — (c), illustrate the contribution of state variables to different modes under $V_{ac}-\Phi$, $V_{ac}-\mathrm{P}$, and $P-Q$ control conditions, respectively, with a constant voltage source. In the $V_{ac}-\Phi$ control condition (Figure 2), dominant contributions are observed from variables like rotor angle (Φ), flux in D- winding (psiD), and flux in Q-winding (psiQ), particularly in critical modes 3, 4, 5, and 6, highlighting a concentrated influence of generator-related dynamics.

In contrast, the $V_{ac}-\mathrm{P}$ control condition (Figure 2) shows a broader spread of participation across modes, with significant contributions from variables such as flux in x-winding (psix), excitation flux (psie), and speed, reflecting a more distributed interaction between state variables and modes.

Meanwhile, the $P-Q$ control condition (Figure 6(c)) exhibits a much more uniform distribution of participation factors across modes, effectively leveraging a wider range of state variables, including rotor angle, fluxes (psiD, psiQ, psix), and excitation flux, which enhances interaction with both dominant and non-dominant modes. The $P-Q$ control strategy's broader and more balanced participation across modes aligns with its observed superiority in improving small-signal stability, as evidenced by significant eigenvalue shifts and increased damping ratios. This highlights the robustness of $P-Q$ control in addressing stability challenges by engaging a wider spectrum of dynamic variables, offering improved overall system performance compared to $V_{ac}-\Phi$ and$V_{ac}-\mathrm{P}$ control strategies.

4.2 Case-II: Variation of solar PV penetration level

In the second case study, a solar PV system has been connected at bus 6, replacing the constant voltage source. The PV system is integrated through an inverter that implements a $P-Q$ control algorithm, known for its superior performance in maintaining system stability. To evaluate the impact of PV penetration on grid stability, the PV penetration level at bus 6 has been varied. A significant observation

from this study is that PV systems inherently lack inertia. As the penetration level of PV increases, the overall system inertia diminishes. This reduction in inertia adversely affects system stability, as evident from the eigenvalue data presented in Table 4. For example, in Mode 14, the real part of the eigenvalue Re(λ) shifts progressively from -0.19 to -0.11 as the PV penetration level increases from 10 MW (6 Mvar) to 100 MW (60 Mvar). A similar trend is observed in Mode 15. This shift of eigenvalues toward the right indicates a reduction in system stability.

Furthermore, the damping ratio decreases with increasing PV penetration. In Mode 14 and Mode 15, the damping ratio declines from 0.825 to 0.756 as PV penetration increases. This behavior is attributed to the diminishing system inertia, which makes the grid more susceptible to instability. The eigenvalue plot (Figure 8) and the participation matrix (Figure 9) corroborate these findings, showing that higher PV penetration levels lead to a less stable system. Therefore, as the level of PV integration increases, it is critical to adopt measures to mitigate the resulting stability challenges.

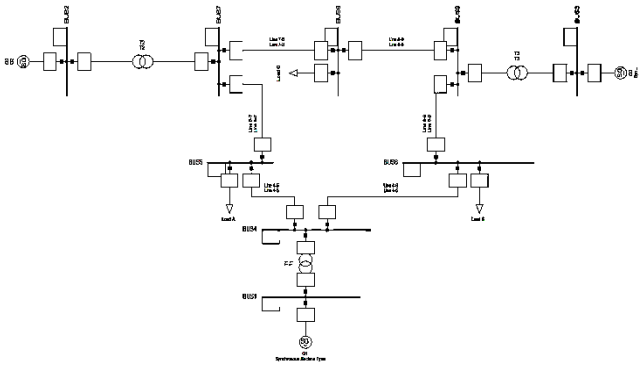

Figure 7: Western System Coordinated Council (WSCC) 3- machine, 9-bus system

Table 4. Eigenvalue and damping ratio with variable PV penetration level.

Mode No.	PV Penetration Level	Eigen Value $\lambda_i = \sigma_i + J\omega_i$	Damping Ratio
14	10 MW, 6 Mvar	$-0.19 + 0.135i$	0.825
	50 MW , 12 Mvar	$-0.17 + 0.118i$	0.822
	100 MW, 60 Mvar	$-0.11 + 0.096i$	0.756
15	10 MW, 6 Mvar	$-0.19 - 0.135i$	0.825
	50 MW , 12 Mvar	$-0.17 - 0.118i$	0.822
	100 MW, 60 Mvar	$-0.11 - 0.096i$	0.756
17	10 MW, 6 Mvar	$-0.144 + 0i$	1
	50 MW , 12 Mvar	$-0.063 + 0i$	1
	100 MW, 60 Mvar	$-0.094 + 0i$	1
18	10 MW, 6 Mvar	$-0.103 + 0i$	1
	50 MW , 12 Mvar	$-0.1004 + 0i$	1
	100 MW, 60 Mvar	$-0.074 + 0i$	1

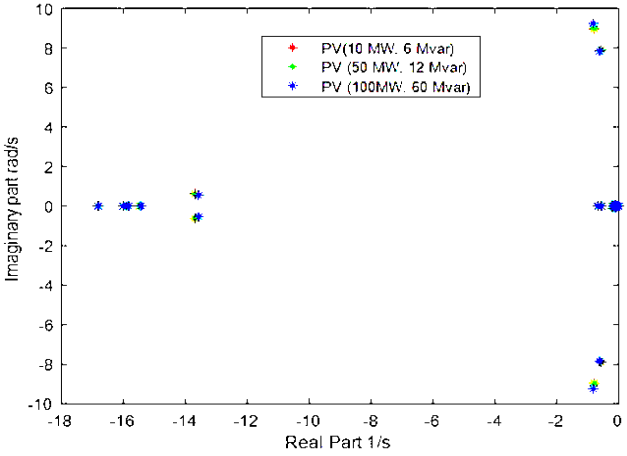

Figure 8: Eigenvalues plot for three different PV penetration level at Bus 6.

The figures (Fig. 10 (a) — (c)) illustrate the participation factor matrices for various modes under increasing PV penetration levels: 10 MW (6 Mvar), 50 MW (12 Mvar), and 100 MW (60 Mvar), respectively. In Fig. 10 (a), corresponding to 10 MW PV penetration, the participation factors are concentrated in a few modes, with notable activity around Modes 2, 6, and 10. The factors exhibit lower magnitudes overall, primarily under 0.4, suggesting minimal interaction of PV with the system modes at this penetration level.

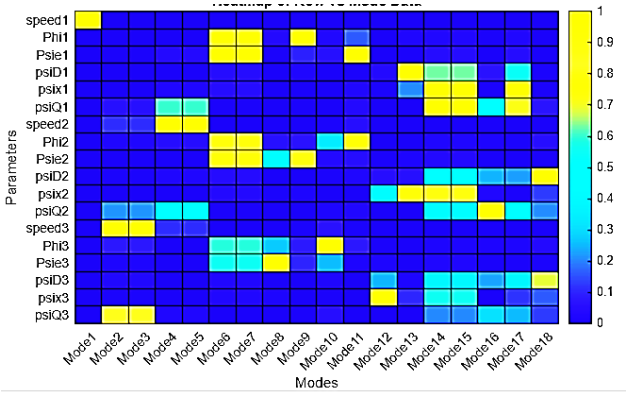

(a)

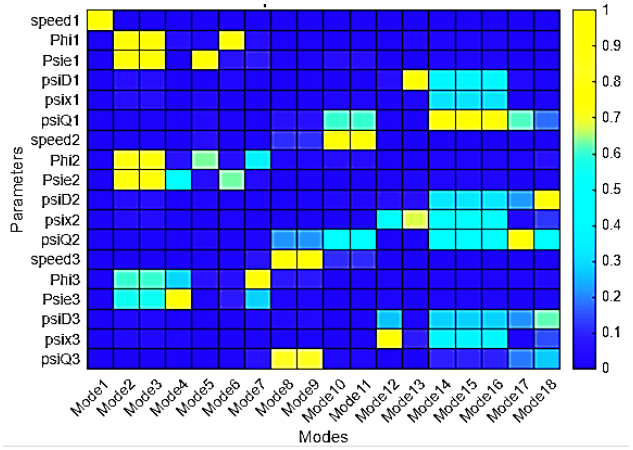

(b)

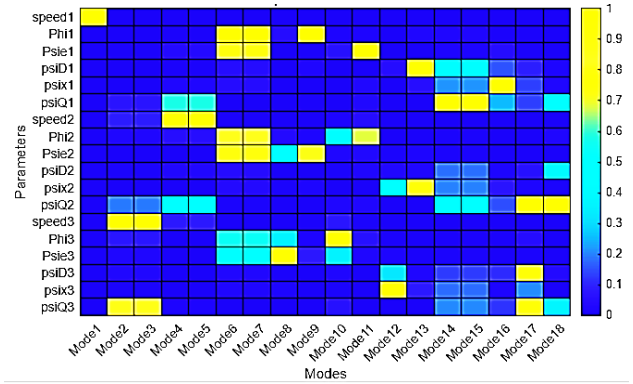

(c)

Figure 9: Matrix of participation factors due to PV penetration (a) 10 MW, 6 Mvar (b) 50 MW, 12 Mvar and (c) 100 MW, 60 Mvar.

In Figure 9 (b), at 50 MW penetration, the intensity of participation factors increases significantly, especially in Modes 3, 6, and 14, with magnitudes ranging from 0.5 to 0.7. This indicates an escalation in PV's influence on system dynamics as penetration grows, with a redistribution of dominance across modes.

In Figure 9 (c), at 100 MW penetration, participation factors expand across multiple modes, including Modes 2, 7, 9, and 17, with some values exceeding 0.8. This widespread distribution highlights the profound effect of high PV penetration on system modal dynamics, potentially introducing new stability challenges. These observations underline a clear trend: as PV penetration increases, its impact on the system becomes more extensive and pronounced, emphasizing the need for adaptive control strategies to manage dynamic interactions and maintain system stability effectively.

4.3 Case-III: Solar PV and Variation of integrated BESS size

To address the reduction in system inertia caused by solar PV integration, a BESS has been deployed alongside the solar PV system at bus 6. The BESS in this study is modeled in $P-Q$ control mode using a PWM converter, enabling independent active and reactive power exchange for grid support. Unlike synchronous machines, it does not provide rotational inertia but contributes synthetic inertia via fast control loops that respond to frequency deviations. The low power factor (PF = 0.51) assumption for both PV and BESS represent a stress-test condition, consistent with IEEE 1547-2018 and IEEE P2800 provisions for non-unity PF operation during voltage regulation, weak-grid support, or disturbance events. This deliberate choice allows the analysis to capture system dynamics under reactive-power-dominant operation, providing a rigorous evaluation of stability. In this analysis, the solar PV output is fixed at 100 MW and 60 Mvar, while the BESS size is varied between 20 MW (10 Mvar) and 50 MW (5 Mvar) to assess its impact on system stability.

Table 5. Eigenvalues and damping ratio with battery integration with PV at Bus 6.

Mode No.	Battery Size	Eigen Value $\lambda_i = \sigma_i + J\omega_i$	Damping Ratio
6	20 MW, 10 Mvar	$-13.55 + 0.516i$	0.99
	50 MW, 5 Mvar	$-13.56 + 0.527i$	0.99
7	20 MW, 10 Mvar	$-13.55 - 0.516i$	0.99
	50 MW, 5 Mvar	$-13.56 - 0.527i$	0.99
15	20 MW, 10 Mvar	$-0.087 + 0.096i$	0.672
	50 MW, 5 Mvar	$-0.098 - 0.095i$	0.72
16	20 MW, 10 Mvar	$-0.087 - 0.096i$	0.672
	50 MW, 5 Mvar	$-0.182 + 0i$	1

As shown in Table 5, the integration of a larger BESS significantly improves the stability of dominant modes such as 6, 7, 15, and 16. For instance, in mode 15, the real part of the eigenvalue Re(λ) shifts from -0.087 to -0.098 as the BESS size increases. A similar leftward shift is observed in Mode 16, where Re(λ) changes from -0.087 to -0.182. Additionally, the damping ratio improves, indicating enhanced stability.

For example, the damping ratio in mode 15 increases from 0.672 to 0.72 with higher BESS integration, and in Mode 16, it improves from 0.672 to 1. The enhanced performance is attributed to the inertial support provided by the BESS, which compensates for the reduced inertia caused by high PV penetration. Consequently, the stability of the grid improves significantly, as corroborated by the eigenvalue plot in Figure 10. This highlights the importance of BESS in mitigating the adverse effects of renewable energy integration on grid stability.

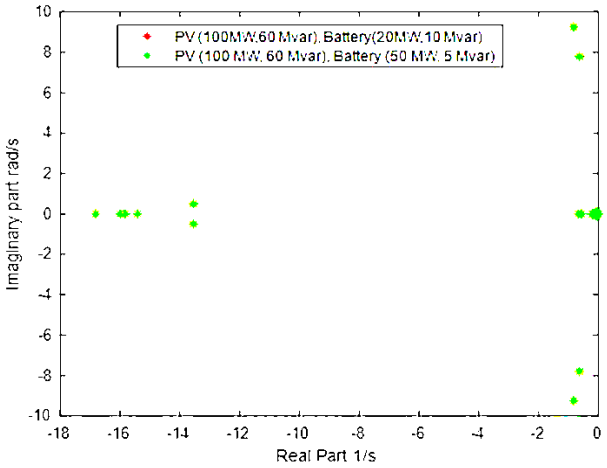

Figure 10: Eigenvalues plot due to battery penetration with solar PV at Bus-6

The two figures, Figure 11 (a) and Figure 11 (b), depict the matrices of participation factors for different configurations of a combined PV and BESS.

In both cases, the PV system is rated at 100 MW and 60 Mvar, while the battery capacities differ: 20 MW with 10 Mvar in Figure 11 (a) and 50 MW with 5 Mvar in Figure 11 (b). These matrices show the contributions of various system states (phi, psiD, psiQ, psix, psie, and speed) to the system's dynamic modes (Mode 1 to Mode 18).

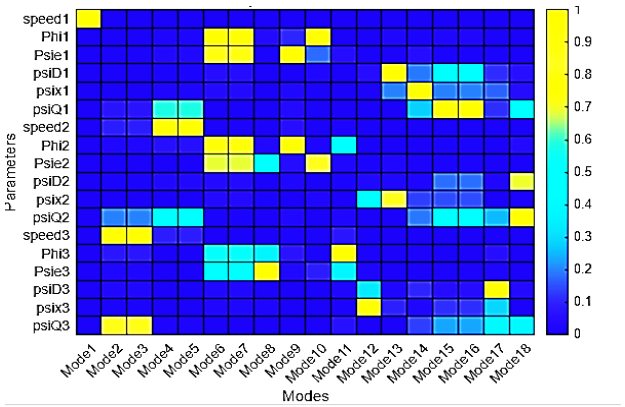

(a)

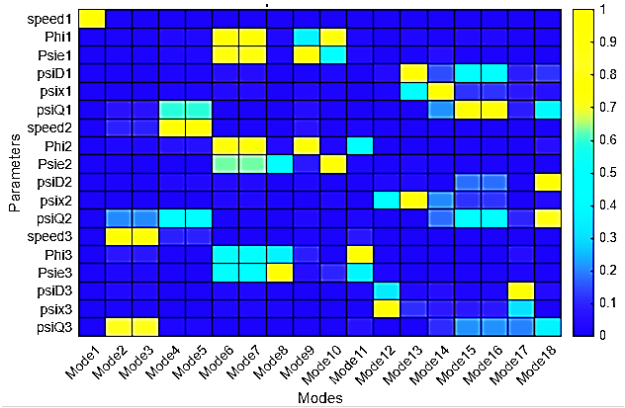

(b)

Figure 11: Matrix of participation factors with PV (100 MW, 60 Mvar) & BESS (a) 20 MW, 10 Mvar and (b) 50 MW, 5 Mvar

In Figure. 11 (a), higher participation factors are observed in Modes 3, 6, and 15 for several states, indicating these modes play a critical role in system behavior under this configuration. For instance, the state "phi" shows a strong interaction with Mode 6, while "psiQ" and "psie" exhibit notable contributions to Mode 15. Similarly, "speed" exhibits increased participation in Modes 3 and 6. The distribution of the participation factors is spread across multiple modes, but the intensity is concentrated in specific state-mode pairs, suggesting a dominant influence on those dynamics. In Figure 11 (b), the increased battery capacity (50 MW, 5 Mvar) results in noticeable changes in the distribution of participation factors. Modes 7 and 12 exhibit heightened activity compared to Figure 11 (a), with states such as "psiQ" and "psix" showing significant contributions. For example, the state "psiQ" demonstrates strong interaction with Mode 7, while "psix" and "psie" have more prominent participation in Mode 12. Additionally, "speed" shows altered contributions, with its influence becoming more distributed across Modes 9, 12, and 16 compared to Figure 11 (a).

These changes indicate that increasing the battery capacity significantly impacts the system's modal behavior. The shifts in dominant modes and state contributions underscore the role of battery sizing in modulating system dynamics and enhancing stability. This comparison highlights the critical influence of combined PV and battery systems on participation factors and provides insights into the dynamic interplay between state variables and system modes under varying configurations.

5. DISCUSSION

This paper presents three case studies conducted on a standard 9-bus system to evaluate stability issues under varying conditions. The first case study investigates the performance of three inverter control strategies— $P-Q$ control, $V_{ac}-\Phi$, and $V_{ac}-P$ under small-signal stability analysis.

The results show that the $P-Q$ control strategy outperforms $V_{ac}-\Phi$ and $V_{ac}-\mathrm{P}$ in terms of stability, primarily due to the superior operation of the VSC with built-in current controllers, as discussed in Section 2.4. Analytical evaluation of the control loop constants demonstrates the effectiveness of $P-Q$ control in optimizing proportional gains (k_p, k_{iq}) and integrator time constants (T_{ip}, T_{iq}), resulting in a distinct leftward shift in eigenvalues, signifying enhanced damping and system inertia.

The superior performance of the $P-Q$ control strategy can be theoretically attributed to its decoupled control of active (P) and reactive (Q) power, allowing independent modulation of real and reactive

components through the $d-q$ reference frame. In this configuration, the d-axis current directly influences active power, while the q-axis current controls reactive power. This separation minimizes cross-coupling between voltage and frequency responses, enhancing dynamic stiffness and improving damping of oscillatory modes. In contrast, $V_{ac}-\Phi$ and $V_{ac}-\mathrm{P}$ control depend on voltage-angle or voltage-power coupling, where interactions between voltage magnitude and phase introduce slower dynamic responses and potential instability under weak-grid conditions. Hence, the $P-Q$ strategy results in higher damping ratios and eigenvalue shifts toward the left-half plane, consistent with small-signal stability improvement.

For instance, the eigenvalue of mode 3 for $V_{ac}-\Phi$ control was $-0.62+9.607i$ with a damping ratio of 0.063, while $V_{ac}-\mathrm{P}$ control yielded $-0.62+9.589i$ (ζ = 0.064). In contrast, the $P-Q$ inverter control strategy achieved $-14.79+0.668i$ with an exceptionally high damping ratio of 0.998, confirming its superior small-signal performance.

The second case study examines varying solar PV penetration levels. Since PV systems lack mechanical inertia, increasing their penetration reduces overall system inertia and stability. For mode 15, eigenvalues shifted from $-0.19+0.135i$ (10 MW PV) to $-0.11+0.096i$ (100 MW PV), while damping ratios decreased from 0.825 to 0.756—indicating a rightward pole shift and reduced stability as PV penetration increases.

To mitigate these inertia-related stability issues, the third case study integrates a BESS alongside PV. Increasing the BESS size from 20 MW to 50 MW shifted the eigenvalue of mode 16 from $-0.087-0.096i$ to $-0.182+0i$, improving the damping ratio from 0.672 to 1.0, thus confirming its strong stabilizing influence.

The superior performance of BESS arises from its ability to emulate virtual inertia and provide fast frequency and voltage support. The converter-based BESS reacts almost instantaneously to power imbalances by modulating active and reactive power through its control loops, enhancing damping and reducing frequency excursions. The coordinated action of its active/reactive power control loops and PWM converter dynamics allows rapid adjustment to grid disturbances, improving overall dynamic stability. Overall, the findings demonstrate that combining the $P-Q$ control strategy with optimally sized BESS significantly enhances small-signal stability in PV-integrated power systems by compensating for reduced inertia and improving damping performance across dominant modes.

6. CONCLUSION

This study investigated the impact of inverter control strategies, solar PV penetration, and Battery Energy Storage System (BESS) integration on the small-signal stability of the WSCC 9-bus system. Three inverter control methods—$V_{ac}-\Phi$, $V_{ac}-\mathrm{P}$, and $P-Q$—were analyzed using modal and participation factor analysis to assess their influence on system damping and dynamic performance. The results revealed that the $P-Q$ control strategy provides the most significant improvement in stability, demonstrating a clear eigenvalue shift from $-0.62+9.607i$ ($V_{ac}-\Phi$) and $-0.62+9.589i$ ($V_{ac}-\mathrm{P}$) to $-14.79+0.668i$ ($P-Q$), with the damping ratio increasing markedly from 0.063 to 0.998. This improvement confirms the effectiveness of $P-Q$ control in enhancing both inertia emulation and oscillation damping under small disturbances.

The study further examined the effect of increasing PV penetration, which led to a progressive rightward shift in eigenvalues (e.g., $-0.19+0.135i$ to $-0.11+0.096i$) and a reduction in damping ratio from 0.825 to 0.756, indicating that higher PV integration weakens system inertia and stability. To counteract this, BESS integration was analyzed, showing that enlarging BESS capacity from 20 MW to 50 MW shifted eigenvalues from $-0.087-0.096i$ to $-0.182+0i$, improving the damping ratio from 0.672 to 1.0. This demonstrates the crucial role of BESS in restoring system stability through fast active–reactive power control and synthetic inertia support.

Overall, the findings highlight that advanced inverter control strategies—particularly $P-Q$ control—combined with appropriately sized BESS can effectively mitigate the stability challenges introduced by high PV penetration. These results provide practical insight into the design of resilient, low-inertia power systems, ensuring improved damping, frequency regulation, and voltage support in future renewable-dominated grids.

ACKNOWLEDGMENTS

The authors would like to thank MIST for providing the necessary facilities and technical support required to successfully conduct the experimental investigations of this study.

DATA AVAILABILITY STATEMENT

Datasets generated during the current study are available from the corresponding author upon reasonable request.

FUNDING DECLARATION

This research was self-funded.

ETHICS APPROVAL

This study is an engineering experimental investigation. The MIJST Research Ethics Committee has confirmed that formal ethical approval was not required.

ETHICS, CONSENT TO PARTICIPATE, AND CONSENT TO PUBLISH

Not applicable.

COMPETING INTERESTS

The authors declare that they have no competing interests.

AUTHOR CONTRIBUTIONS

Author 1: Md. Mahadi Hasan - visualization, original draft preparation, review and editing of the manuscript and final approval of the manuscript.

Author 2: Md. Imranul Hasan Emon - Formal analysis, experimental investigation, data acquisition, and review and editing of the manuscript, drafting the paper.

Author 3: Hasan Monir - Conceptualization, methodology development, Supervision, project administration, and final approval of the manuscript.

Author 4: Md Ahsan Kabir - Drafting the initial manuscript and critical revision of the manuscript.

ARTIFICIAL INTELLIGENCE ASSISTANCE STATEMENT

Portions of this manuscript were assisted by an artificial intelligence language model (ChatGPT, OpenAI). The tool was used solely for language editing, text refinement, and clarity improvement. All content, data interpretation, analysis, conclusions, and final decisions were generated, verified, and approved by the authors. The authors take full responsibility for the accuracy and integrity of the manuscript.

CONFLICT OF INTEREST DECLARATION

The authors declare that they have no conflicts of interest.

REFERENCES

Ali, Z. M., Ćalasan, M., Jurado, F., & Aleem, S. H. A. (2024). Complexities of power quality and harmonic-induced overheating in modern power grids studies: Challenges and solutions. IEEE Access.

Akatsuka, M., Hara, R., Kita, H., Ito, T., Ueda, Y., & Saito, Y. (2010, June). Estimation of battery capacity for suppression of a PV power plant output fluctuation. In 2010 35th IEEE Photovoltaic Specialists Conference (pp. 000540–000543). IEEE.

Alias, F., & Singh, M. (2021). Damping sensitivity analysis and optimized battery controller for small-signal stability enhancement in wind penetrated networks. Sustainable Energy, Grids and Networks, 26, 100441.

Aljarrah, R., Fawaz, B. B., Salem, Q., Karimi, M., Marzooghi, H., & Azizipanah-Abarghooee, R. (2024). Issues and challenges of grid-following converters interfacing renewable energy sources in low inertia systems: A review. IEEE Access, 12, 5534–5561.

Biroon, R. A., Pisu, P., & Schoenwald, D. (2020, February). Large-scale battery energy storage system dynamic model for power system stability analysis. In 2020 IEEE Texas Power and Energy Conference (TPEC) (pp. 1–5). IEEE.

Boscaino, V., Ditta, V., Marsala, G., Panzavecchia, N., Tinè, G., Cosentino, V., … & Di Cara, D. (2024). Grid-connected photovoltaic inverters: Grid codes, topologies and control techniques. Renewable and Sustainable Energy Reviews, 189, 113903.

Cheah-Mane, M., Egea-Alvarez, A., Prieto-Araujo, E., Mehrjerdi, H., Gomis-Bellmunt, O., & Xu, L. (2023). Modeling and analysis approaches for small-signal stability assessment of power-electronic-dominated systems. Wiley Interdisciplinary Reviews: Energy and Environment, 12(1), e453.

Chen, Q., Bu, S., & Chung, C. Y. (2023). Small-signal stability criteria in power electronics-dominated power systems: A comparative review. Journal of Modern Power Systems and Clean Energy, 12(4), 1003–1018.

Das, T., & Aliprantis, D. C. (2008, November). Small-signal stability analysis of power system integrated with PHEVs. In 2008 IEEE Energy 2030 Conference (pp. 1–4). IEEE.

Daud, M. Z., Mohamed, A., Wanik, M. C., & Hannan, M. A. (2012, December). Performance evaluation of grid-connected photovoltaic system with battery energy storage. In 2012 IEEE International Conference on Power and Energy (PECON) (pp. 337–342). IEEE.

DIgSILENT. (2011). DIgSILENT PowerFactory Technical Reference Documentation: PWMConverter ElmVsc, ElmVscmono. DIgSILENT GmbH.

Emrani, A., Achour, Y., Sanjari, M. J., & Berrada, A. (2024). Adaptive energy management strategy for optimal integration of wind/PV system with hybrid gravity/battery energy storage using forecast models. Journal of Energy Storage, 96(112613), 112613.

Gali, V., Jamwal, P. K., Gupta, N., & Kumar, A. (2023). Multimode control strategy to improve the power quality and autonomy of PV–Wind–BESS-based microgrid using harmonic frequency adaptive observer filter. Electric Power Systems Research, 225, 109786.

Hamid, A. K., Mbungu, N. T., Elnady, A., Bansal, R. C., Ismail, A. A., & AlShabi, M. A. (2023). A systematic review of grid-connected photovoltaic and photovoltaic/thermal systems: Benefits, challenges and mitigation. Energy & Environment, 34(7), 2775–2814.

Hill, C. A., Such, M. C., Chen, D., Gonzalez, J., & Grady, W. M. (2012). Battery energy storage for enabling integration of distributed solar power generation. IEEE Transactions on Smart Grid, 3(2), 850–857.

International Renewable Energy Agency. (2022, July). Renewable power remains cost-competitive amid fossil fuel crisis. https://www.irena.org/...

Iyer, V. M., Gulur, S., & Bhattacharya, S. (2018). Small-signal stability assessment and active stabilization of a bidirectional battery charger. IEEE Transactions on Industry Applications, 55(1), 563–574.

Jamal, T., Urmee, T., Calais, M., Shafiullah, G. M., & Carter, C. (2017). Technical challenges of PV deployment into remote Australian electricity networks: A review. Renewable and Sustainable Energy Reviews, 77, 1309–1325.

Jerkø, A. (2014). Reactive Power and Voltage Control of Offshore Wind Farms (Master's thesis).

Kåberger, T. (2018). Progress of renewable electricity replacing fossil fuels. Global Energy Interconnection, 1(1), 48–52.

Kiasari, M., Ghaffari, M., & Aly, H. H. (2024). A comprehensive review of the current status of smart grid technologies for renewable energies integration

and future trends: The role of machine learning and energy storage systems. Energies, 17(16), 4128.

Koohi-Kamali, S., Rahim, N. A., & Mokhlis, H. (2014). Smart power management algorithm in microgrid consisting of photovoltaic, diesel, and battery storage plants considering variations in sunlight, temperature, and load. Energy Conversion and Management, 84, 562–582.

Lu, Z., Chen, Y., & Fan, Q. (2021). Study on feasibility of photovoltaic power to grid parity in China based on LCOE. Sustainability, 13(22), 12762.

Makarov, Y. V., Lu, S., Ma, J., & Nguyen, T. B. (2008). Assessing the value of regulation resources based on their time response characteristics (No. PNNL-17632). Pacific Northwest National Laboratory.

McGinn, D., Galán, E. M., Green, D., CEC, C. E. C., Junfeng, L., Hinrichs-Rahlwes, R., … & Lins, C. (2013). REN21 Renewables 2013 Global Status Report.

Muriuki, J. K., Muriithi, C. M., Ngoo, L., & Nyakoe, G. N. (2016). Assessment of VSC-HVDC system for transient stability improvement of a power system with large wind power injection.

Powerfactory, D. (2011). Powerfactory user's manual. DIgSILENT GmbH. Powerfactory, D. (2011). Powerfactory user's manual. DIgSILENT GmbH. Milan.

Qiao, L., Xue, Y., Kong, L., & Wang, F. (2024). Small-signal stability analysis for large-scale power electronics-based power systems. IEEE Open Access Journal of Power and Energy, 11, 280–292.

Ali, S. Z., Nahian, M. K., & Hoque, M. E. (2023). Chapter 19—Extraction of cellulose from agro-industrial wastes. In S. Bhawani, A. Khan, & F. Ahmad (Eds.), Extraction of Natural Products from Agro-Industrial Wastes (pp. 319–348). Elsevier. https://doi.org/10.1016/B978-0-12-823349-8.00013-7

Ram, M., Child, M., Aghahosseini, A., Bogdanov, D., Lohrmann, A., & Breyer, C. (2018). A comparative analysis of electricity generation costs from renewable, fossil fuel and nuclear sources in G20 countries for the period 2015–2030. Journal of Cleaner Production, 199, 687–704. \

REN21. (2023). Renewables 2023 Global Status Report. https://www.ren21.net/...

Renné, D. S. (2022, February). The opportunities and challenges for 100% renewable energy. In Sustainable Energy Development and Innovation (pp. 495–503). Springer.

Roser, M. (2020). Why did renewables become so cheap so fast? Our World in Data.

Shaw, P., & Kumar, P. (2016, November). Small signal stability analysis of a battery connected standalone photovoltaic system. In 2016 7th India International Conference on Power Electronics (IICPE) (pp. 1–6). IEEE.

Shivashankar, S., Mekhilef, S., Mokhlis, H., & Karimi, M. (2016). Mitigating methods of power fluctuation of photovoltaic (PV) sources—A review. Renewable and Sustainable Energy Reviews, 59, 1170–1184.

Tavakoli, A., Saha, S., Arif, M. T., Haque, M. E., Mendis, N., & Oo, A. M. (2020). Impacts of grid integration of solar PV and electric vehicle on grid stability, power quality and energy economics: A review. IET Energy Systems Integration, 2(3), 243–260.

Teng, J. H., Luan, S. W., Lee, D. J., & Huang, Y. Q. (2012). Optimal charging/discharging scheduling of battery storage systems for distribution systems interconnected with sizeable PV generation systems. IEEE Transactions on Power Systems, 28(2), 1425–1433.

Vetoshkin, L., & Müller, Z. (2021). A comparative analysis of a power system stability with virtual inertia. Energies, 14(11), 3277.

Wiser, R. H., Mills, A. D., Seel, J., Levin, T., & Botterud, A. (2017). Impacts of variable renewable energy on bulk power system assets, pricing, and costs.

Zeng, J., Zhang, B., Mao, C., & Wang, Y. (2006). Use of battery energy storage system to improve power quality and stability of wind farms. In 2006 International Conference on Power System Technology (pp. 1–6). IEEE.